

Development of a Degradation-Conscious Physics-Based Lithium-Ion Battery Model for Use in Power System Planning Studies

Yang Li ^{a,*}, Mahinda Vilathgamuwa ^a, San Shing Choi ^a, Troy W. Farrell ^b, Ngoc Tham Tran ^a, Joseph Teague ^b

^a School of Electrical Engineering and Computer Science, Queensland University of Technology, 2 George St, Brisbane, QLD 4000, Australia

^b School of Mathematical Sciences, Queensland University of Technology, 2 George St, Brisbane, QLD 4000, Australia

* Corresponding author. Email address: yangli@ieee.org (Y. Li).

Abstract: A computationally-efficient and reliable method is developed to permit the simultaneous assessment of both the short- and long-term performance of lithium-ion battery in power system planning studies. Toward this end, a physics-based equivalent circuit model of the lithium-ion battery is derived in which side reaction-induced degradation of the battery is included. Whence a computational procedure is developed to enable the parametric values of the circuit elements in the equivalent circuit model to be automatically updated as the battery operates. The resulting model allows the increase in the internal resistance and the decrease in the energy storage capacity of the battery to be determined, based solely on the information of the power flows at the battery terminals. Dynamic simulation results obtained using the developed equivalent circuit model are shown to be in close agreement with those obtained from well-established electrochemical models, but at a much reduced computational burden.

Keywords: lithium-ion battery, battery energy storage system, physics-based model, degradation model, power system planning studies.

1. Introduction

Battery energy storage is increasingly being recognized as essential for modern electric power systems which contain significant amount of renewable generation. Of the various types of battery, lithium-ion (Li-ion) battery has become the most prominent candidate in such application [1] [2]. A case in point is the 100-MW/129-MWh Li-ion battery energy storage system (BESS) which operates in conjunction with the 315-MW Hornsdale wind farm in South Australia [3]. Renewable generations, such as that based on wind and sunlight, tends to be uncertain and can seriously compromise the security and reliability of power supply as a result [4]. The role of the BESS is to alleviate such undesirable impacts on the power systems, and the BESS have to be judiciously designed at the planning stage so as to comply with stipulated technical and economic requirements [5].

System-level design of the BESS usually involves two aspects. First, *operational planning* is the strategization of the short-term (from several hours up to several days) power flows at the BESS plant terminals and the design of charging/discharging pattern of the BESS. Various approaches to BESS design have been developed aiming to achieve such short-term control objectives as power smoothing, peak shaving, and/or dispatch scheduling. In [6], a BESS control strategy and the real-time power allocation method have been developed for photovoltaic and wind generation by modifying the smoothing target according to the monitored BESS state of charge. To enable the renewable generators to emulate the ability of the traditional thermal units in providing reliable power dispatch, operational strategies based on feedback control [7], model predictive control [8], and rule-based control [9] have been proposed, the purpose of which is to minimize the generation schedule tracking error. The short-term dispatch schedule for a dual-BESS scheme has been studied in [10] for a wind farm, with the objective to minimize

the number of the switch-over between the two battery banks. In these works, the storage capacity and power rating of the BESS have been assumed known a priori. On the other hand, the aspect of *battery sizing* is to determine suitable BESS energy storage capacity and power rating during the design and planning stage of the BESS. The aim of the study is to ensure the long-term (say, several years) technical and economic requirements imposed on the BESS can be met. As the design objective for short-term operation affects the results of battery sizing study, the above-mentioned two aspects of the BESS design have to be considered simultaneously. Toward this end, the BESS design can always be formulated as a system-level optimization problem, with some form of cost-benefit analysis. For example: the dispatch strategy and BESS capacity are determined by maximizing a defined service lifetime/cost index, so that the short-term dispatchability of a wind farm is achieved [11]. On the other hand, by treating the BESS as a power smoothing device or as an energy buffer to be utilized to reduce the degradation on the quality of electricity supply due to the uncertain renewable sources, the optimal BESS capacity can be determined using a cost-benefit analysis, as has been done in [12]. A variable-interval reference signal optimization approach and a fuzzy control charging/discharging scheme are proposed in [13] for BESS to smoothen the generated wind power, and the optimal BESS capacity is determined by minimization of the BESS annualized cost. In [14], the optimal planning of distributed BESS in active distribution networks has been investigated with the consideration of reactive power support and short-term network reconfiguration, the optimal power/energy capacities and location has been obtained using mixed-integer second-order-cone programming. The optimal placement, capacity and operation of BESS in conjunction with high penetration of photovoltaic in distribution network has been studied in [15] to effectively limit the voltage rise. A method to maximize the profit of wind farm is presented in [16] to

incorporate BESS, and the optimal BESS design is obtained using dynamic programming. A statistical approach to determine the capacity and the charging/discharging strategy for battery-supercapacitor hybrid storage system is discussed in [17], with the aim to achieve a dispatchable wind farm. Operational planning for a wind–battery system is carried out in [18] using a modified min-max dispatch method. A coordinated operational dispatch and capacity determination scheme for a BESS-wind farm is proposed in [19], with the view to mitigate the fluctuation and stochastic nature of the wind resources through changing the wind farm output power reference value between the optimistic and pessimistic forecast scenarios. Based on Sequential Monte Carlo simulation technique, a wind farm incorporated with BESS is designed in [20] to track the generation schedule while the optimal BESS capacity and control strategy is studied by considering the real-time pricing of electricity in [21]. In all these works [11]–[21], precise prediction of the lifetime of the battery has been considered an important long-term factor for the economic evaluation. One common concern pertaining to the aforementioned works is that empirical measurements of battery lifetime, such as that based on maximum cycle number or Ah-throughput, have been used to predict the BESS end-of-life (EOL). Unfortunately, these relatively simple battery lifetime determination methods have not been proven to be entirely reliable for Li-ion based batteries. This is because the degradation of the batteries are known to be dependent of the potential, current direction, current magnitude, depth of discharge, temperature, amongst other factors [22], [23].

Furthermore, the optimization procedure referred to in the planning studies requires BESS model which is able to accurately predict both the short- and long-term battery performance, but at acceptable computational burden. As befitting the short-term role of energy buffer, the amount of the energy stored in the BESS is often evaluated, subjected to hard constraints such as the BESS energy capacity and power rating [20]. In this connection, the BESS dynamic behavior can be studied using battery equivalent circuit models (ECMs), as has been done in [6]–[10]. The main reasons for using this type of empirical models are that ECMs are intuitive to the researchers in the field of electrical engineering, while the short-term battery performance can be readily analyzed using well-established circuit theory. Additional constraints such as applied current and terminal voltage limits can be readily included, as part of the optimization design procedure. Unfortunately, as the capability of Li-ion battery to efficiently store or release energy reduces with battery usage, the degradation of BESS performance has to be included. Although for online control purpose, the parametric values of the circuit components in the ECMs could be adjusted to fit the observed battery performance, this approach requires complex set of data to be extracted from laboratory experiments or staged tests [24]. The suitability of such an approach to battery modeling at the planning study stage of the BESS is doubtful because the experimental or staged test conditions can be significantly different from that encountered in the field [25].

In contrast to the ECM and based on electrochemical and

thermodynamic principles, various physics-based Li-ion battery models have been developed in recent years for the purpose of battery cell design [26]. These models do consider the internal behavior and the major causes of battery aging, such as that due to side reactions and mechanical stresses, and are indeed capable of predicting accurately both the short- and long-term performance of the battery cell [27]. Also, intensive investigations have identified the side reactions in the negative electrode are the major cause of Li-ion cell degradation [28]. Various phenomena due to the side reactions, such as the loss of active material and the increase of the depletion layer, can be readily incorporated into these physics-based models [29]. The physics-based models have been further simplified in the attempt to balance between model accuracy and computational efficiency, so that they can be incorporated into advanced battery management systems for online prediction of battery cell performance and lifetime [30], [31]. Notwithstanding these developments however, these simplified first-principle models are still too complex and are incompatible for use in the planning and capacity determination studies of the BESS.

In consideration of [6]–[31], the aim of the present work is to develop a reliable and practical method to predict Li-ion BESS performance for system-level BESS design and planning studies. Toward this end, a physics-based ECM of the Li-ion battery is derived from an electrochemical model such that the quantitative links between the electrochemical process of the Li-ion battery and the circuit dynamics are established. The long-term impacts of side reactions on battery storage capacity and internal resistance are included in the ECM. Whence a numerical procedure that is compatible with system-level optimization procedure is developed to automatically update the parametric values of the physics-based ECM circuit parameters as the battery cell degradation progresses. The resulting model allows accurate and rapid prediction of the behavior of Li-ion battery, thanks to the recent research outcomes in battery electrochemistry and circuit theory. To the best knowledge of the authors, the present investigation is the first reported work to incorporate physics-based Li-ion model in the design and planning of grid-connected BESS.

Accordingly, the remaining contents are organized as follows: Section 2 presents the modeling considerations of grid-connected BESS and the essence of an electrochemical model of Li-ion battery, from which Section 3 develops a physics-based ECM with the incorporation of the major degradation mechanism. A reduced-order ECM suitable for system-level studies is also derived. Several indices are then developed in Section 4 to provide quantitative measures of the energy storage and power delivery capabilities of the battery which can be directly used for BESS design. Section 5 includes a comparison of reported experimental data, simulation results obtained using well-established electrochemical battery models with those from the developed ECMs. Examples of the application of the developed models are also given. Main findings are included in Section 6.

2. Electrochemical Model of Li-Ion Battery

2.1 Some Preliminary Considerations

In order to develop the Li-ion battery model which shall be computationally efficient and yet sufficiently accurate for use in power system planning studies, the following assumptions have been made.

Low C-rate: It is well recognized BESS is suitable for use to support intra- and inter-day energy management of power grids [32]. For such an application, the maximum C-rate of the BESS is often limited to a much lower level compared to that used in mobile applications, such as in electric vehicles [33]. Indeed in the abovementioned literature [6]-[21], the capacity of the BESS is such that the BESS operating C-rate is usually limited to no higher than 1C. Under this constrained C-rate, laboratory results show that the effects of the spatial variations of local concentration and potential in the electrolyte are negligible [34], and the behavior of electrolyte can be described using a lumped resistance [25]. In this condition, major internal electrochemical dynamics and external characteristics of the cell can be explained using the single particle model (SPM) [25] [27]. More would be said about the SPM in the next sub-section.

Constant temperature: the low C-rate current on a battery bank generates much less heat per cell than that encountered in high C-rate applications. Also as space and weight are of less important design factors for the grid-connected BESS than that for use in electric vehicles, the BESS can be housed in an environmentally-controlled facility and the battery operating temperature can be readily controlled [33]. Accordingly, in this study, the operating temperature of the BESS is assumed to be maintained at a suitably constant level and the impact on battery performance due to any variations in the temperature is negligible.

Degradation due to side reactions: Although various causes of Li-ion battery degradation have been identified (see e.g., [35, 36]), for the purpose of BESS planning studies, the degradation mechanisms that occur in extremely unsuitable or stressed operating conditions shall not be considered. These conditions, including overcharge, overdischarge and over-temperature, should be avoided through the careful design and operations of the BESS. Hence, attention of the present study is only directed towards the most common degradation mechanisms encountered during the normal operations of the BESS. In this connection, the major cause of the Li-ion cell degradation has been identified as the consequence of the irreversible side reactions between lithium ions and electrolyte solvent species in the negative electrode of all types of Li-ion battery cells. Indeed this degradation mechanism has been considered in the design of battery management systems in [28, 35, 36]. Accordingly, the side reactions-induced degradation shall be included in the present study. Finally, accelerated aging can be observed near the EOL of Li-ion battery [22, 37], especially when the battery is operating at high temperature [38]. Operating the battery under such an unreliable state is, however, considered not advisable for power system application. Hence this operating condition shall be excluded in the present investigation.

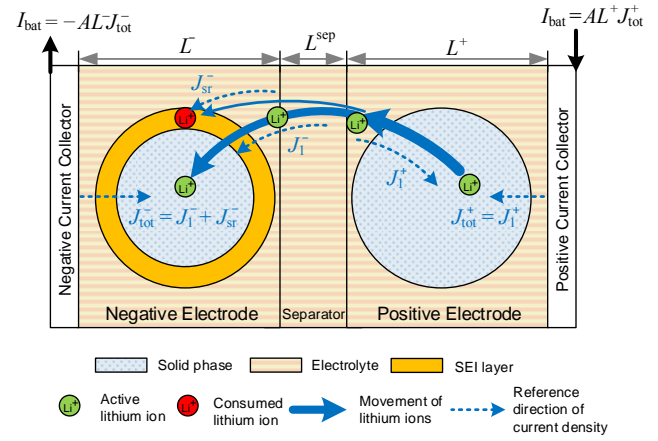


Fig. 1. Schematic of the single particle model of Li-ion cell during the charging process: the lithium ions diffusion from the inner region of the positive electrode particle to its surface, react and transport to the negative electrode. Side reactions occur at the surface of the particle in the negative electrode, and SEI layer grows to cause capacity fade.

2.2 Single Particle Model

A schematic diagram of the SPM of Li-ion battery cell is presented in Fig. 1. It shows the positive electrode (relevant quantities are denoted by the superscript “+” sign), the negative electrode (denoted by “-”), the separator (denoted by “sep”), and the two current collectors. In the SPM, the lithium ions in each electrode are assumed to be stored in a spherical particle. This particle represents the solid phase in the porous electrode with lattice structure. When the battery is charging, as shown in Fig. 1, most of the lithium ions in the positive electrode will first diffuse to the surface of the particle, transport across the separator via the electrolyte, and then diffuse into the particle in the negative electrode. The reverse process occurs during discharging. These *reversible* intercalation/deintercalation processes are referred to as the *main reactions* hereafter. The volume-averaged current density due to this movement of lithium ions is denoted as $J_1^\pm(t)$. Note that the superscript “ \pm ” represent the quantity for both electrodes.

In contrast to the main reactions, the *side reactions* are pertaining to the process when a small amount of the lithium ions react with the solvent species, producing a thin film at the solid-electrolyte interphase (SEI) in the negative electrode. Side-reaction current density in the negative electrode is denoted as $J_{sr}^-(t)$, as shown in Fig. 1. The relationship between $J_1^\pm(t)$, $J_{sr}^-(t)$ and the applied current $I_{bat}(t)$ is given by

$$J_{tot}^+(t) = J_1^+(t) = I_{bat}(t) / (AL^+) \quad (1a)$$

$$J_{tot}^-(t) = J_1^-(t) + J_{sr}^-(t) = -I_{bat}(t) / (AL^-) \quad (1b)$$

where $J_{tot}^\pm(t)$, L^\pm and A are the total current density, the width, and the cross-sectional area of the electrode respectively. Here the direction of the current density terms are defined as positive when lithium ions are entering the particle, as indicated by the dashed lines in Fig. 1.

2.3 Short-Term Dynamics due to the Main Reactions

The short-term study of BESS is closely related to the charging/discharging process of Li-ion battery which

accompanies the main reactions. The main reactions cause the Li-ion concentration in the particle to vary radially and with time. This dynamic process is governed by Fick's law of diffusion equation expressed in spherical coordinates. By applying a polynomial profile approximation, the Fick's law of diffusion equation can be reduced to the following ordinary differential equations [39]:

$$\dot{\theta}_{s,avg}^{\pm}(t) = -\frac{1}{c_{s,max}^{\pm}} \frac{a^{\pm}}{\varepsilon_s} j_1^{\pm}(t) = -\frac{3}{c_{s,max}^{\pm} R_p} j_1^{\pm}(t) \quad (2a)$$

$$\dot{q}_{s,avg}^{\pm}(t) = -\frac{30D_s^{\pm}}{(R_p^{\pm})^2} q_{s,avg}^{\pm}(t) - \frac{45}{2(R_p^{\pm})^2} j_1^{\pm}(t) \quad (2b)$$

$$j_1^{\pm}(t) = -\frac{35D_s^{\pm} c_{s,max}^{\pm}}{R_p^{\pm}} (\theta_{ss}^{\pm}(t) - \theta_{s,avg}^{\pm}(t)) + 8D_s^{\pm} q_{s,avg}^{\pm}(t) \quad (2c)$$

where $\theta_{s,avg}^{\pm}(t)$ and $\theta_{ss}^{\pm}(t)$ are the volume-averaged stoichiometry and the stoichiometry at the particle surface, respectively. Stoichiometry refers to the respective Li-ion concentration, normalized with respect to the theoretical maximum Li-ion concentration $c_{s,max}^{\pm}$. Furthermore, R_p^{\pm} denotes the radius of the spherical particle, D_s^{\pm} is the solid phase diffusivity, ε_s^{\pm} is the volume fraction of the solid phase, $a^{\pm} = 3\varepsilon_s^{\pm}/R_p^{\pm}$ is the specific area of the electrode, $q_{s,avg}^{\pm}(t)$ is the average concentration flux, $j_1^{\pm}(t) = J_1^{\pm}(t)/(Fa^{\pm})$ is the pore-wall molar flux, and F is the Faraday constant.

Next, the potential $\Phi_s^{\pm}(t)$ at the terminal of each electrode is given by

$$\Phi_s^{\pm}(t) = U_{ss}^{\pm} + \eta_1^{\pm}(t) \pm \frac{r_f^{\pm}}{AL^{\pm} a^{\pm}} I_{bat}(t) + \Phi_e^{\pm}(t) \quad (3)$$

The various terms on the RHS of (3) are now described. The equilibrium potential U_{ss}^{\pm} of the electrode appears as the first term. U_{ss}^{\pm} is expressed as a function $f_{s\pm}(\cdot)$ of the surface stoichiometry θ_{ss}^{\pm} . $f_{s\pm}(\cdot)$ is determined by the characteristics of the electrode materials and it can be obtained experimentally. $f_{s\pm}(\cdot)$ of several types of commonly-used electrode in commercial Li-ion batteries are shown in Appendix A. The analytical expressions of $f_{s\pm}(\cdot)$ are assumed known in this work. The second term $\eta_1^{\pm}(t)$ on the RHS of (3) is the activation overpotential of the main reactions and it is expressed as

$$\eta_1^{\pm}(t) = \frac{2R_g T}{F} \sinh^{-1} \left(\frac{F j_1^{\pm}(t)}{2i_0^{\pm}(t)} \right) \quad (4)$$

$$i_0^{\pm}(t) = r_{eff}^{\pm} c_{s,max}^{\pm} \sqrt{c_e^0 \theta_{ss}^{\pm}(t) (1 - \theta_{ss}^{\pm}(t))} \quad (5)$$

where R_g is the universal gas constant, T is the cell temperature, $i_0^{\pm}(t)$ is exchange current density of the main reactions, r_{eff}^{\pm} is the electrode rate coefficient, and c_e^0 is the average Li-ion concentration in the electrolyte. The third term on the RHS of (3) represents an overpotential when battery current flow through the SEI film resistance r_f^{\pm} . The last term $\Phi_e^{\pm}(t)$ on the RHS of (3) is the electrolyte potential. The potential difference $\Phi_e^+(t) - \Phi_e^-(t)$ between the positive and negative electrodes is modelled as

$$\Phi_e^+(t) - \Phi_e^-(t) = \frac{1}{2A} \left(\frac{L^+}{\kappa_{eff}^+} + \frac{2L^{sep}}{\kappa_{eff}^{sep}} + \frac{L^-}{\kappa_{eff}^-} \right) I_{bat}(t) \quad (6)$$

where κ_{eff} represents the effective electrolyte conductivity.

Finally, the terminal voltage of the battery $V_{bat}(t)$ is

$$V_{bat}(t) = \Phi_s^+(t) - \Phi_s^-(t) + R_{col} I_{bat} \quad (7)$$

where R_{col} is the lumped resistance of the current collectors.

2.4 Long-Term Dynamics due to the Side Reactions

The *irreversible* side-reaction current density in the negative electrode is modelled using Tafel equation [28] [31], i.e.

$$J_{sr}^-(t) = -i_{0,sr} a^- \exp \left(-\frac{F \eta_{sr}^-(t)}{2R_g T} \right) \quad (8)$$

where $\eta_{sr}^-(t)$ and $i_{0,sr}$ are the activation overpotential and the exchange current density of the side reactions, respectively. Similar to $\eta_1^+(t)$ in (3), $\eta_{sr}^-(t)$ is given by

$$\eta_{sr}^-(t) = \Phi_s^-(t) - \Phi_e^-(t) - U_{sr,ref}^- + \frac{r_f^-(t)}{AL^- a^-} I_{bat}(t) \quad (9)$$

where the equilibrium potential $U_{sr,ref}^-$ of the side reactions can be assumed to be constant, consistent with the approach used in [27-29, 31].

The side reactions can cause the evolution of model parameters. As the main purpose of the present study is to use the existing electrochemical models to derive system-level Li-ion battery model, the increase of SEI film resistance in the negative electrode is considered due to the presence of J_{sr}^- , i.e.

$$r_f^-(t) = -\frac{M_f}{\rho_f \kappa_f} \frac{1}{Fa^-} \int_0^t J_{sr}^-(\tau) d\tau + r_{f,0}^- \quad (10)$$

where M_f , ρ_f , κ_f and $r_{f,0}^-$ are the molecular weight, density, ionic conductivity, and initial resistance of the SEI film. The SEI film resistance r_f^+ in the positive electrode is considered constant [24].

On the other hand, the impact of side reactions on the decrease of volume fraction number ε_s^- due to the loss of active materials has been reported [29]. More will be said about this aspect of parametric variation in Sub-section 3.2.

As explained in Section 2.2, the growth of the SEI film is the product of the side reactions that consumes lithium ions and solvent species. It will lead to slow degradation of Li-ion cell in the forms of capacity fade and power fade [40], and which affects the long-term performance of the BESS. In the next section, a physics-based Li-ion battery ECM will be derived based on (1)–(10). Following that, the effect of degradation will be investigated using the developed ECM.

3 Physics-Based Equivalent Circuit Models

3.1 Derivation of a Physics-Based Equivalent Circuit Model for Li-Ion Battery

It is intuitive and convenient to use equivalent circuits in the field of electrical engineering for system design and indeed, using ECM is a popular pathway toward studying the behavior of BESS. However, conventional empirically-derived ECMs do not provide information on the various battery internal states which can affect battery long-term performance. In view of this shortcoming, a degradation-conscious physics-based ECM will now be derived from (1)–(10).

First, perform the change of variables from $\theta_{s,avg}^\pm(t)$, $q_{s,avg}^\pm(t)$ and $j_1^\pm(t)$ to voltages and current quantities. These latter quantities are easier to relate physically, in the context of electrical circuits:

$$V_1^\pm = f_{s\pm}(\theta_{s,avg}^\pm) \quad (11)$$

$$V_2^\pm(t) = -\left(\frac{8R_p^\pm f_{s\pm}'(\theta_{s,avg}^\pm)}{35c_{s,max}^\pm}\right) q_{s,avg}^\pm(t) \quad (12)$$

$$I_1^\pm(t) = AL^\pm J_1^\pm(t) = AL^\pm F a^\pm j_1^\pm(t) \quad (13)$$

Following the detailed derivation given in Appendix B, the solid-phase diffusion equation (2) can then be converted to

$$\dot{V}_1^\pm(t) = \frac{1}{C_1^\pm} I_1^\pm(t) \quad (14a)$$

$$\dot{V}_2^\pm(t) = -\frac{1}{R_2^\pm C_2^\pm} V_2^\pm(t) + \frac{1}{C_2^\pm} I_1^\pm(t) \quad (14b)$$

$$U_{ss}^\pm(t) = V_1^\pm(t) + V_2^\pm(t) + R_1^\pm I_1^\pm(t) \quad (14c)$$

where the R and C parameters are expressed as

$$\left. \begin{aligned} C_1^\pm(\theta_{s,avg}^\pm) &= \frac{AL^\pm F \varepsilon_s^\pm c_{s,max}^\pm}{-f_{s\pm}'(\theta_{s,avg}^\pm)} & C_2^\pm &= \frac{7}{12} C_1^\pm \\ R_1^\pm(\theta_{s,avg}^\pm) &= \frac{-f_{s\pm}'(\theta_{s,avg}^\pm)}{AL^\pm F \varepsilon_s^\pm c_{s,max}^\pm} \frac{(R_p^\pm)^2}{105D_s^\pm} & R_2^\pm &= 6R_1^\pm \end{aligned} \right\} \quad (15)$$

Next, the activation overpotential $\eta_{1,1}^\pm(t)$ can be treated as the consequence of the presence of a resistance $R_{\eta,1}^\pm$. It is shown in [41] that under low C-rate condition,

$$R_{\eta,1}^\pm(\theta_{s,avg}^\pm) = \frac{\eta_{1,1}^\pm(t)}{I_1^\pm(t)} \approx \frac{1}{AL^\pm a^\pm} \frac{R_g T}{F} \frac{1}{i_0^\pm(\theta_{s,avg}^\pm)} \quad (16)$$

Substituting (3), (6), (14c) and (16) into (7) yields the terminal voltage

$$V_{bat}(t) = V_1^+ - V_1^- + V_2^+ - V_2^- - (R_{\eta,1}^- + R_1^-) I_1^-(t) + (R_f^+ + R_f^- + R_{\eta,1}^+ + R_e + R_{col} + R_1^+) I_{bat}(t) \quad (17)$$

where the SEI resistance R_f^\pm and the electrolyte resistance R_e are defined as

$$R_f^\pm = \frac{r_f^\pm}{AL^\pm a^\pm} \quad (18)$$

$$R_e = R_e^+ + R_e^{sep} + R_e^- = \frac{1}{2A} \left(\frac{L^+}{\kappa_{eff}^+} + \frac{2L^{sep}}{\kappa_{eff}^{sep}} + \frac{L^-}{\kappa_{eff}^-} \right) \quad (19)$$

For the side reactions, define a resistance $R_{\eta,sr}^-$ to associate the activation overpotential $\eta_{sr}^-(t)$ with the side reaction current I_{sr}^- , viz.,

$$R_{\eta,sr}^- = \frac{\eta_{sr}^-(t)}{I_{sr}^-(t)} = \frac{2R_g T}{F} \frac{\ln[-J_{sr}^-(t)/(i_{0,sr}^- a^-)]}{AL^- J_{sr}^-(t)} \quad (20)$$

where I_{sr}^- is defined herewith as

$$I_{sr}^-(t) = AL^- J_{sr}^-(t) \quad (21)$$

Equation (8) shows that $J_{sr}^- < 0$. Whence from (21), the direction of flow of I_{sr}^- is independent of that of the applied current I_{bat} . This is because the irreversible side reactions are

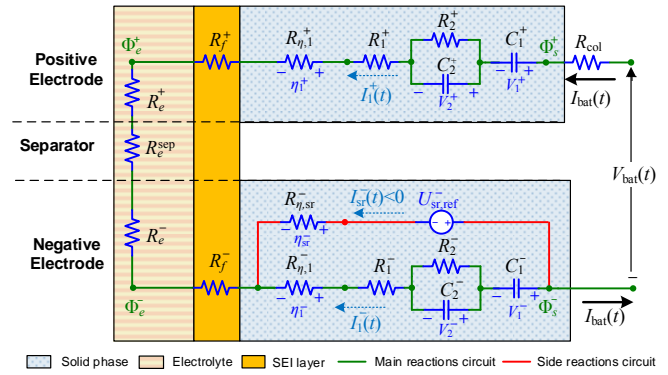


Fig. 2. A degradation-conscious physics-based equivalent circuit derived from single particle model of Li-ion battery. The circulating current I_{sr}^- in the negative electrode is the result of side reactions. The flow direction of I_{sr}^- is always opposite to the reference direction indicated by the dotted arrow.

Table 1

Physical meanings of the various voltages shown in the ECM.

Voltage Quantities	Physical Meanings
V_1^\pm	OCP of the electrode
$V_1^+ - V_1^-$	OCV of the battery
$V_2^\pm + R_1^\pm I_1^\pm$	Solid-phase overpotential due to Li-ion diffusion
η_1^\pm	Activation overpotential of the main reaction
η_{sr}^-	Activation overpotential of the side reaction
$R_f^\pm I_1^\pm$	Overpotential due to the SEI film resistance
$V_1^\pm + V_2^\pm + R_1^\pm I_1^\pm$	Equilibrium potential U_{ss}^\pm of the electrode
$U_{ss}^\pm + \eta_1^\pm + R_f^\pm I_1^\pm$	Potential Φ_s^\pm of the electrode

solely due to the interactions between the lithium ions and solvent, and are not affected by intercalation/deintercalation.

Finally, using (3), (9) and (20), one obtains

$$R_{\eta,sr}^- I_{sr}^-(t) + U_{sr,ref}^- = U_{ss}^- + \eta_1^-(t) \quad (22)$$

Accordingly from (14), (17) and (22), the equivalent circuit shown in Fig. 2 is derived. The expressions of the R and C parameters of the derived ECM are given by (15), (16) and (18)–(20), while the currents are expressed by (13) and (21). Furthermore, the slow evolution of the SEI resistance R_f^- shall be governed by side reaction current I_{sr}^- , described by (10), (18) and (21). The key point is that the voltages appearing across the various circuit elements in the ECM can be identified with the intercalation kinetics, ion diffusion and electric potentials. These relationships are summarized in Table 1. Specifically, the capacitor voltage V_1^\pm represents the open-circuit potential (OCP) of the electrode, and the battery open-circuit voltage (OCV) is the difference between V_1^+ and V_1^- . In the ECM, C_1^\pm is the main energy storage component, while R_1^\pm , R_2^\pm and C_2^\pm pertain to the diffusion of lithium ions in the solid phase. The remaining difference between V_{bat} and the OCV is caused by the solid phase Li-ion diffusion and the various internal resistances.

3.2 Capacity Fade

The developed circuit shown in Fig. 2 can be used to explain the phenomenon of capacity fade of Li-ion battery. Using (11)

and (15), the amount of electric charges Q_1^\pm stored in the capacitor C_1^\pm can be calculated as:

$$Q_1^+(t) = \frac{AL^+ F \varepsilon_s^+ c_{s,\max}^+}{3600} (\theta_{0\%}^+ - \theta_{s,\text{avg}}^+(t)) \quad (23)$$

$$Q_1^-(t) = \frac{AL^- F \varepsilon_s^- c_{s,\max}^-}{3600} (\theta_{100\%}^- - \theta_{s,\text{avg}}^-(t)) \quad (24)$$

Q_1^+ is defined as zero when $\theta_{s,\text{avg}}^+ = \theta_{0\%}^+$; it corresponds to the state of the stoichiometry of the positive electrode when the battery is fully-discharged at the begin-of-life (BOL) stage of the battery operation, and correspondingly $\theta_{s,\text{avg}}^- = \theta_{0\%}^-$ and $Q_1^- = Q_{\max,0}$. Simultaneously Q_1^- is defined as zero when $\theta_{s,\text{avg}}^- = \theta_{100\%}^-$, the state of the stoichiometry of the negative electrode when the battery is fully-charged at the BOL of the battery and correspondingly, $\theta_{s,\text{avg}}^+ = \theta_{100\%}^+$ and $Q_1^+ = Q_{\max,0}$. Typically the V_1^\pm vs. Q_1^\pm profile curves of a battery at the BOL stage of battery operations are as shown in Fig. 3(b) and Fig. 3(c). They are shown by the black solid curves in the figure and are similar to the function $f_{s\pm}(\theta_{s,\text{avg}}^\pm)$ given in (11). This is because of the linear relationship between Q_1^\pm and $\theta_{s,\text{avg}}^\pm$, as conveyed by (23) and (24). The OCV vs. Q_1^+ curve in Fig. 3(a) can be obtained according to $\text{OCV} = V_1^+ - V_1^-$. As an illustration, points P, A, and B in Fig. 3 govern the state of the battery OCV, V_1^+ and V_1^- respectively when the battery is at the BOL.

If the side reactions are ignored, $I_{\text{sr}} = 0$, and suppose the battery is charged from the BOL stage. The stored charges in C_1^+ and C_1^- change by the amount ΔQ_1^+ and ΔQ_1^- respectively. Clearly $\Delta Q_1^+ = -\Delta Q_1^-$ as a result of charge conservation. The new operating states of the battery OCV, V_1^+ and V_1^- will be P', A', and B' in Fig. 3 respectively, as the consequence of the changes in the stored charges.

Now include the side reactions. As shown in Fig. 3(c), the potential of the negative electrode V_1^- is always lower than the side reaction reference voltage $U_{\text{sr,ref}}^-$. So the side reaction current $I_{\text{sr}}(t)$ will thus circulate in the negative electrode circuit and in the direction opposite to that shown in Fig. 2. Hence, C_1^- will receive an amount of electric charge Q_{loss}^- due to the circulating I_{sr}^- . Q_{loss}^- (in Ah) can be calculated, as follows:

$$Q_{\text{loss}}^-(t) = -\frac{1}{3600} \int_0^t I_{\text{sr}}^-(\tau) d\tau + Q_{\text{loss},0}^- \quad (25)$$

Consequently, while the operating point of C_1^+ remains at A', the operating point of C_1^- will now move to the left by the amount Q_{loss}^- along the Q_1^- axis, to reach the point B''. The state of charge on C_1^- is now closer to the limit $Q_{\max,0}$ by the amount Q_{loss}^- ; the capacity for C_1^- for it to be fully discharged has been reduced by the amount Q_{loss}^- . So although the ability for C_1^+ to fully discharge has not been affected by the side reactions, the ability of the battery as a whole to discharge has been reduced due to loss of lithium ions. As a consequence, the V_1^- vs. Q_1^- curve will move to the right by amount of Q_{loss}^- , as shown in Fig. 3(c). The new OCV curve is obtained as shown in Fig. 3(a) since $\text{OCV} = V_1^+ - V_1^-$. The new V_1^+ and OCV are depicted by red solid curves.

By the same reasoning, it can also be concluded that due to the side reactions, there is a reduction in the charge storage capacity of the battery during the discharging process as long as the side reactions occurs. This loss in storage capacity is an

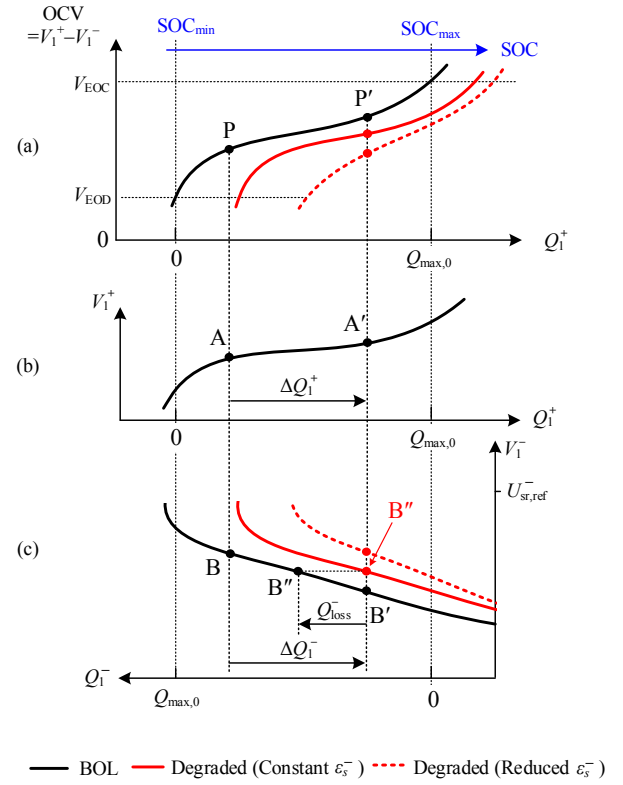


Fig. 3. Typical relationships of (a) OCV vs Q_1^+ ; (b) OCP of the positive electrode V_1^+ vs Q_1^+ ; (c) OCP of the negative electrode V_1^- vs Q_1^- . The black solid curves correspond to battery at BOL stage. The red solid curves correspond to the case after the side reactions have occurred but the variation of volume fraction number ε_s^- has not been considered. With the variation in ε_s^- included, the red solid curves move to the right and appear as the red dotted curves.

irreversible process and is commonly referred to as capacity fade of Li-ion battery. Even when the BESS is not in service and $I_{\text{bat}} = 0$, the circulating current I_{sr}^- continues to flow which leads to the battery continuously losing the storage capacity. Indeed, the presence of the side reactions has been identified as one of the major causes for the so-called self-discharge of Li-ion cell [29]. Thus unlike the empirical ECMs derived from observed external characteristics, the physics-based ECM shown in Fig. 2 allows these internal electrochemical behaviors of the Li-ion battery to be explained and accounted for.

The above analysis can be readily extended to investigate the effect of the variation of other parameters on capacity fade. For example and as alluded to in Section 2.4, if the reduction of the solid phase volume fraction ε_s^- as a results of the loss of active material is taken into consideration, the following equation taken from [29] can be incorporated into the ECM:

$$\varepsilon_s^-(t) = k_{\text{iso}} \frac{M_f}{\rho_f} \frac{1}{F} \int_0^t J_{\text{sr}}^-(\tau) d\tau + \varepsilon_{s,0}^- \quad (26)$$

where k_{iso} is a dimensionless constant describing the rate of reduction of ε_s^- . As the amount of charge $Q_1^-(t)$ remains unchanged, according to (24), $\theta_{s,\text{avg}}^-(t)$ will increase in proportion to the reduction of ε_s^- . Since $V_1^- = f_{\text{sr}}^-(\theta_{s,\text{avg}}^-)$, this will cause a shrinking of the V_1^- vs. Q_1^- curve, shown by the

red dotted line in Fig. 3(c). It in turn will cause further OCV change and capacity fade as shown in Fig. 3(a).

3.3 A Reduced-Order Equivalent Circuit Model

In this sub-section, the proposed 4th-order ECM in Fig. 2 will be simplified and a computationally efficient solution procedure will be developed for grid-connected BESS design studies.

First, for system-level study, the short-term transient due to the Li-ion diffusion can be ignored. It is shown in the authors' previous work [42] and the derivation in Appendix B that the parallel RC components in Fig. 2 can be approximated by a resistance of $6R_1^\pm$.

Next, from Fig. 3 it can be readily seen that $Q_1^+(t)$ and $Q_1^-(t)$ shall satisfy

$$Q_1^+(t) + Q_1^-(t) = Q_{\max,0} + Q_{\text{loss}}^-(t) \quad (27)$$

Considering the side-reaction current I_{sr}^- is much lower than the main-reaction current I_1^+ and I_1^- , within a relatively short simulation time step T_s , the increase in $Q_{\text{loss}}^-(t)$ calculated using (25) tends to be much smaller than the variations in $Q_1^+(t)$ and $Q_1^-(t)$. So $Q_{\text{loss}}^-(t)$ can be considered constant in (27) and thus $Q_1^-(t)$ and $Q_1^+(t)$ become dependent variables. To simplify notation, hereafter $Q_1^+(t)$ is denoted by the state variable z to indicate the *state of intercalation*.

It can be seen from (15) and (16) that some of the RC parameters are functions of $\theta_{s,\text{avg}}^\pm$. Furthermore, using (23), (24) and (27), the linear relationships between $\theta_{s,\text{avg}}^\pm(t)$ and $Q_1^\pm(t)$ can be readily derived. Hence, the RC parameters can now be expressed as functions of z . Whence the series-connected components can be combined to yield

$$R_{\text{eq}1}(z) = R_{\text{col}} + R_e + R_f^+ + R_{\eta,1}^+(z) + 7R_1^+(z) + R_f^- \quad (28)$$

$$R_{\text{eq}2}(z) = R_{\eta,1}^-(z) + 7R_1^-(z) \quad (29)$$

Two additional equivalent components are also defined for use in latter analysis:

$$C_{\text{eq}}(z) = C_1^+(z)C_1^-(z) / (C_1^+(z) + C_1^-(z)) \quad (30)$$

$$R_{\text{eq}}(z) = R_{\text{eq}1}(z) + R_{\text{eq}2}(z) \quad (31)$$

Next, the incorporation of side reaction circuit imposes an algebraic constraint to the ECM via (16) and (20)–(22). Instead of using time-consuming iterative method to solve the nonlinear simultaneous equations, it is proposed to replace the side reaction branch by a current source I_{sr}^- . I_{sr}^- can be expressed as an explicit function f_{sr} of z and I_{bat} , i.e.

$$I_{\text{sr}}^-(t) = f_{\text{sr}}(z, I_{\text{bat}}) \quad (32)$$

The expression of f_{sr} is given in Appendix B. Based on the above simplification, the reduced-order equivalent circuit model (RO-ECM) shown in Fig. 4 is obtained.

However, over a longer period T_d , the increase in $Q_{\text{loss}}^-(t)$ can be significant. $Q_1^+(t)$ and $Q_1^-(t)$ will have to be evaluated using (27) by taking into account the change in $Q_{\text{loss}}^-(t)$. $R_{\text{eq}}(z)$, $C_{\text{eq}}(z)$ and $f_{\text{sr}}(z, I_{\text{bat}})$ will have to be updated as a result. In this case, $Q_{\text{loss}}^-(t)$ represents another state variable which is evaluated using (25). In this work, each T_d interval is selected to correspond to a particular *state of degradation* of the Li-ion battery. Henceforth, the state of degradation is denoted by an

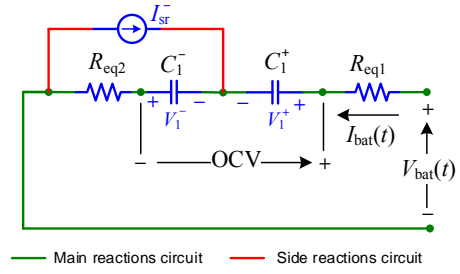


Fig. 4. A reduced-order physics-based ECM for Li-ion battery. The parallel RC components in Fig. 2 are replaced by pure resistances for planning studies.

index k , with $k = 0$ when the battery is at the BOL stage. Furthermore, k would be attached as a subscript to each of the battery parameters to signify its association with the k -th state of degradation. For example, $R_{\text{eq}}(z)$ and $f_{\text{sr}}(z, I_{\text{bat}})$ would be denoted as $R_{\text{eq},k}(z)$ and $f_{\text{sr},k}(z, I_{\text{bat}})$, respectively. Also, from (10), (21), (25) and (26), it can be shown that the circuit parameters impacted by the cell degradation can now be expressed as functions of $Q_{\text{loss},k}^-$, i.e.

$$R_{f,k}^- = R_{f,0}^- + k_{\text{SEI}} Q_{\text{loss},k}^- \quad (33)$$

$$\varepsilon_{s,k}^- = \varepsilon_{s,0}^- - k_{\text{AM}} Q_{\text{loss},k}^- \quad (34)$$

where $k_{\text{SEI}} = 3600M_f / [(k_p \rho_f F) \cdot (AL^- a)^2]$ and $k_{\text{AM}} = 3600k_{\text{iso}}M_f / (\rho_f F AL^-)$.

3.4 Solution Procedure for the Reduced-Order Equivalent Circuit Model in System-Level Studies

In view of the fast intercalation dynamics due to the main reactions and the slow degradation dynamics due to the side reactions, a dual time-step solution procedure to simulate the Li-ion battery behavior for a given battery input power $P_{\text{bat}}(t)$ is now proposed, as follows.

Initialization: Starting from the instance when the battery is at its BOL ($k = 0$) state, with the given initial values of the state variable of intercalation z_0 and $Q_{\text{loss},0}^- = 0$, calculate the initial circuit parameters such as $R_{f,0}^-$ and $\varepsilon_{s,0}^-$. The initial terminal voltage is the corresponding OCV.

Step 1: Calculate the battery current $I_{\text{bat}}(t)$, viz., $I_{\text{bat}}(t) = P_{\text{bat}}(t) / V_{\text{bat}}(t - T_s)$.

Step 2: Calculate the state variable $z(t)$ using (35) based on $I_{\text{bat}}(t)$ and $z(t - T_s)$;

$$z(t) = Q_1^+(t) = I_{\text{bat}}(t)T_s / 3600 + z(t - T_s) \quad (35)$$

Step 3: Calculate $V_1^+(t)$ from $z(t)$ using (23) and $f_{s^+}(\cdot)$.

Step 4: Calculate the side reaction current $I_{\text{sr}}^-(t)$ based on $I_{\text{bat}}(t)$ and $z(t)$ using (32);

Step 5: Calculate $Q_{\text{loss}}^-(t)$ using (25);

Step 6: If the end of a T_d interval is reached, let $Q_{\text{loss},k}^- = Q_{\text{loss}}^-(t)$, and perform the following calculations (a), (b), (c) and (d) using $Q_{\text{loss},k}^-$. Otherwise go to **Step 7** directly;

(a) Update the relationship between z and $Q_1^-(t)$ according to (27);

(b) Update the relationships between $Q_1^-(t)$ and $V_1^-(t)$ according to (24) and $f_{s^-}(\cdot)$, if ε_{s^-} is varying;

(c) Update R_f^- according to (18) and (33);

(d) Update the function $f_{\text{sr}}(z, I_{\text{bat}})$ according to the equations (C.1) and (C.2) given in Appendix C;

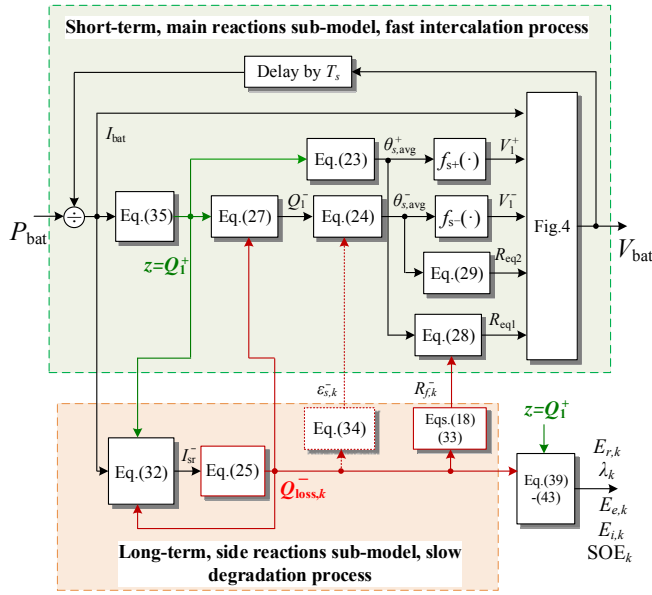


Fig. 5. The general model structure and solution procedure for the developed RO-ECM. $z = Q_1^+$ represents the state of the stored charge level; $Q_{loss,k}^-$ is associated with the state of degradation level and the input to the model is battery power P_{bat} . Terminal voltage V_{bat} is the output of the model. Other outputs regarding the stored energy level and energy capacity used in planning studies can be expressed as functions of Q_1^+ and $Q_{loss,k}^-$, as given in (39)–(43).

Step 7: Calculate the terminal voltage $V_{bat}(t)$ using (17) and $V_1^+(t)$, $V_1^-(t)$, $R_{eq1,k}(z)$, $R_{eq2,k}(z)$, and $I_{bat}(t)$.

Repeat **Steps 1–7** for the next T_s until the end of the simulation period is reached. The block diagram of the developed model and solution procedure is shown in Fig. 5, where the numerical integration uses the time-step T_s for the main reactions sub-model, and T_d for the side reactions sub-model.

4 Analysis of Battery Performance

4.1 Impact of Degradation on Circuit Parameters

Fig. 6(a) shows the relationship between the OCV and $Q_1^+(t)$, i.e. z , of the particular type of Li-ion battery considered in [26, 28, 40]. The curves correspond to the battery at BOL ($k = 0$), at an arbitrary state of degradation k , and at such a degraded state that the battery is considered to have reach its EOL. Also, define herewith the end-of-charge (EOC) state as when the battery OCV_k reaches the pre-specified maximum voltage level V_{EOC} , and the corresponding Q_1^+ is $Q_{1,EOC,k}^+$. Similarly the end-of-discharge (EOD) state occurs when the battery OCV_k is at the pre-specified minimum voltage level V_{EOD} . The corresponding $Q_{1,EOC,k}^+$ and $Q_{1,EOD,k}^+$ are also shown in Fig. 6(a). Whence the battery Ah capacity at the k^{th} state of degradation is defined as

$$Q_{max,k} = Q_{1,EOC,k}^+ - Q_{1,EOD,k}^+ \quad (36)$$

Note that at BOL, $Q_{1,EOD,k}^+ = 0$ and $Q_{1,EOC,k}^+ = Q_{max,k} = Q_{max,0}$. As the battery degrades, both $Q_{1,EOC,k}^+$ and $Q_{1,EOD,k}^+$ have shifted to the right. Interestingly it is observed the right shift in $Q_{1,EOD,k}^+$ is much more pronounced than that of $Q_{1,EOC,k}^+$. A reduction in the Ah capacity $Q_{max,k}$ as defined by (36) is observed.

In order to fairly compare the capacity fade effect and the variation of circuit parameters as the battery degrades, one can shift the OCV curve in Fig. 6(a) toward the left by the amount $(Q_{1,EOC,k}^+ - Q_{max,0})$, so that all the OCV curves intercept the V_{EOC} line at the same point. Next, normalize the horizontal axis based on the battery Ah capacity $Q_{max,0}$ at BOL. The horizontal axis is now expressed as the battery state-of-charge (SOC), i.e.

$$SOC(t) = [Q_1^+(t) - (Q_{1,EOC,k}^+ - Q_{max,0})] / Q_{max,0} \quad (37)$$

The linear relationship between SOC and Q_1^+ shown in (37) is also reflected in Fig. 3, in which SOC_{max} and SOC_{min} are respectively the upper and lower limits of SOC when the battery is at the BOL. The resulting OCV vs. SOC curves are shown in Fig. 6(b), and it can be seen the SOC range between the EOC and EOD reduces as k increases.

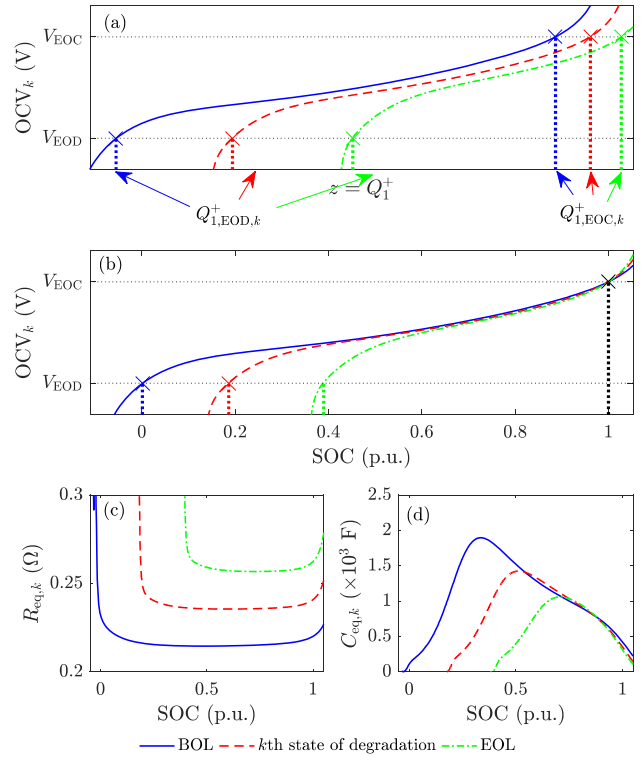


Fig. 6. Functional relationships of (a) OCV_k vs. z , (b) OCV_k vs. SOC, (c) $R_{eq,k}$ vs. SOC, and (d) $C_{eq,k}$ vs. SOC when the battery is at the BOL, k^{th} , and EOL state of degradation.

Furthermore, Fig. 6(c) shows that the overall resistance $R_{eq,k}(SOC)$, as defined by (31), increases significantly with k . This is primarily due to the increase in R_f , the SEI film resistance. At the same time, Fig. 6(d) shows that $C_{eq,k}(SOC)$, as defined by (30), decreases appreciably as k increases. The most severe degradation state shown is that corresponding to the battery EOL condition (defined as $Q_{max,k} = 0.55Q_{max,0}$ in this example). The combination of these trends will have significant bearing in the capability of the battery to efficiently store and convert energy as the battery degrades.

4.2 Feasible Operating Zone

Fig. 7 shows the battery terminal voltage V_{bat} vs SOC curves when the battery is at the BOL state and that at an arbitrary k^{th} state of degradation. The OCV₀(SOC) curve corresponding to the BOL state is the dotted line A₀B₀. Fig. 7 also shows several

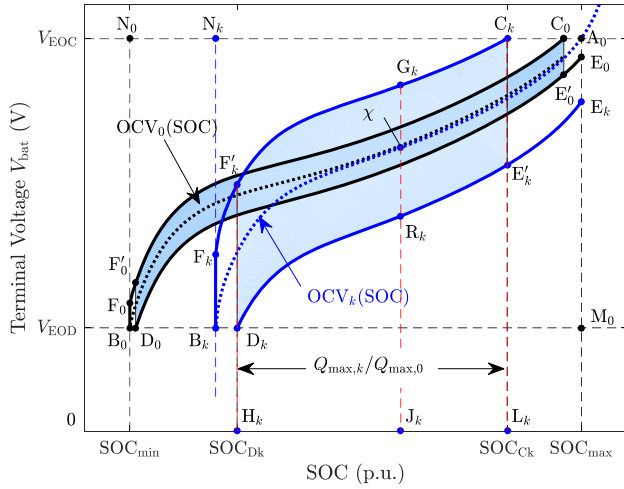


Fig. 7. Li-ion battery feasible operating zone (the shaded area) as impacted by the growth of the SEI film, and the loss of lithium ions and solvent species.

practical limits imposed on the battery operations which are considered in Sub-sections 2.1 and 4.1. The vertical lines N_0B_0 and A_0M_0 denote the minimum and maximum SOC imposed on the battery operations in order to avoid the undesirable over-discharge/over-charge. The horizontal lines N_0A_0 and B_0M_0 prescribe the voltage limits that defined the EOC and EOD states alluded to earlier.

Apart from the constraints placed on the terminal voltage and the SOC, the continuous operating power rating P_r of the battery and the associated power converter is yet another practical limit imposed on the operations of the BESS. V_{bat} at the maximum battery power charging/discharging conditions can be obtained simply by satisfying the equation

$$OCV_k(SOC) \pm (P_r / V_{bat}) R_{eq,k}(SOC) = V_{bat} \quad (38)$$

In Fig. 7, the trajectories F_0C_0 and E_0D_0 correspond to the instances when the battery is at the BOL and it is being loaded under the continuous maximum power charging and discharging conditions respectively. As shown in Fig. 7, a feasible SOC range for the maximum power operation is approximately $[SOC_{min}, SOC_{max}]$. Hence, the shaded area within the boundary $C_0E_0D_0F_0C_0$ prescribes the feasible operating zone (FOZ) of the BESS at BOL. By the same reasoning, when the battery is at the k^{th} state of degradation, the corresponding new FOZ is $C_kE_kD_kF_kC_k$ shown in Fig. 7. The $OCV_k(SOC)$ curve would now intersect the new boundary at A_0 and B_k . According to the analysis shown in Section 4.1, the position of B_k determines the Ah capacity $Q_{max,k}$ defined by (36). Due to the increased resistance $R_{eq,k}$, the vertical distance between the discharging curve E_kD_k and the charging curve F_kC_k becomes wider than that when that battery is at BOL. Thus the feasible SOC range is reduced to $[SOC_{Dk}, SOC_{Ck}]$. SOC_{Ck} and SOC_{Dk} can be calculated using (38) by setting $V_{bat} = V_{EOC}$ and $V_{bat} = V_{EOD}$, respectively. These operating constraints can be used in system studies when designing BESS operational strategy.

4.3 Energy Storage Capacity

For the applications of BESS in grid systems, power flows, stored energy and energy conversion efficiency are of direct interest. In Fig. 4, the capacitor $C_{eq} = C_1^+ || C_1^-$ is the dominant energy storage component in the ECM. For a small change dQ

in the amount of stored charge in C_{eq} , the corresponding change in its stored energy is $dE = V_C \times dQ = OCV \times d(SOC \times Q_{max,0})$. For the battery to be capable of supplying rated power P_r continuously, as the case when developing Fig. 7, the *feasible energy storage capacity* $E_{r,k}$ of the battery at the k^{th} state of degradation is

$$E_{r,k} = Q_{max,0} \int_{SOC_{Dk}}^{SOC_{Ck}} OCV_k(SOC') dSOC' \quad (39)$$

The feasible energy storage capacity $E_{r,0}$ when the battery is at BOL can be calculated by setting $SOC_{Ck} \approx SOC_{max}$ and $SOC_{Dk} \approx SOC_{min}$ into (39). As the battery degradation progresses, the $OCV_k(SOC)$ curve becomes increasingly depressed. Furthermore, in view of the FOZ, as SOC_{Dk} moves to the right of SOC_{min} , while SOC_{Ck} moves to the left of SOC_{max} , the value of the integral term in (39) reduces and $E_{r,0}$ decreases to $E_{r,k}$. Therefore, the ability of the BESS to store energy reduces over time.

Next, introduce the concept of energy storage capacity index λ_k :

$$\lambda_k = E_{r,k} / E_{r,0} \quad (40)$$

λ_k provides a measure of the energy storage capacity of the battery at the k^{th} degradation state relative to that when the battery is at BOL. The value of λ_k would decrease as the battery degrades, which is another way to reflect the capacity fade phenomenon on Li-ion battery as described in Section 3.2.

Also, two additional indices can be introduced to quantify the maximum amount of energy that can feasibly be exported/imported at the BESS terminals at any given time. Consider Fig. 7 again and the SOC of the battery corresponds to that at the arbitrary operating point χ on the $OCV_k(SOC)$ curve. Clearly, the maximum amount of energy that can be *exported* before the BESS reaches its minimum feasible SOC level SOC_{Dk} is

$$E_{e,k}(SOC) = Q_{max,0} \int_{SOC_{Dk}}^{SOC} \left[OCV_k(SOC') - \frac{P_r R_{eq,k}(SOC')}{V_{EOD}} \right] dSOC' \quad (41)$$

Conversely, the maximum amount of energy that can be *imported* by the battery before its SOC arrives at the maximum feasible SOC level SOC_{Ck} is

$$E_{i,k}(SOC) = Q_{max,0} \int_{SOC}^{SOC_{Ck}} \left[OCV_k(SOC') + \frac{P_r R_{eq,k}(SOC')}{V_{EOC}} \right] dSOC' \quad (42)$$

$E_{e,k}(SOC)$ and $E_{i,k}(SOC)$ are proportional to the areas enclosed by the boundaries $R_kD_kH_kJ_kR_k$ and $G_kC_kL_kJ_kG_k$ respectively in Fig. 7. As $R_{eq,k}(SOC)$ and $C_{eq,k}(SOC)$ evolve over time, one can dynamically track the maximum amount of the energy the battery can feasibly be exported or imported at any given time by applying (41) or (42). Such information is most useful in developing operational strategies for the battery, as when for example, the battery attempts to carry out the power smoothing or power dispatch tasks such as those described in [6]-[21].

Another useful index for practical use in BESS design is the state of energy (SOE), which can be defined as

$$SOE_k(t) = \frac{\int_{SOC_{Bk}}^{SOC(t)} OCV_k(SOC') dSOC'}{\int_{SOC_{Bk}}^{SOC_{max}} OCV_k(SOC') dSOC'} \quad (43)$$

where the numerator represents the amount of the stored energy that can be discharged and the denominator is the stored energy capacity. SOC_{Bk} is the SOC at the point B_k .

5 Results and Discussion

5.1 Model Validation

In this sub-section, the developed RO-ECM is to be validated using the experimental data obtained in [43] where it reports that a $LiCoO_2$ battery with 1.8-Ah rated capacity is tested under certain cyclic conditions. In each cycle, firstly, the battery is charged from a given initial stoichiometry. The charging current is constant at 1 A until the battery terminal voltage reaches V_{EOC} of 4.2 V. Then, the terminal voltage is kept constant by reducing the charging current until the current falls below 50mA. The battery is then discharged at the constant 1A level until the battery terminal voltage reaches the cut-off level of about $V_{EOD} = 2.0$ V. Whence the battery is deemed to have completed one charging-discharging cycle and the cycle is then repeated. The electrochemical parametric values for the RO-ECM used in the simulation are given in Table A.1 in Appendix A. The volume fraction is considered constant in this case, consistent with the assumption made in [43].

The simulation results of the battery terminal voltages at the end of the 10th, 300th, 400th and 800th charging-discharging cycles are shown in Fig. 8. The figure clearly indicates that the proposed RO-ECM is able to capture the major effect of the degradation, in the form of the reduction in the discharge capacity as the cycle number increases. For example, the discharge capacity has been reduced from 1.8 Ah at the end of the 10th cycle to some 1.2 Ah at the end of the 800th cycle. Most encouraging, in comparison with the experimental data, the maximum error between the experimental and the predicted discharge capacity is less than 2%. Furthermore, the RO-ECM yields the battery terminal voltage profile which is in good agreement with the experimental measurements throughout the complete discharge process.

5.2 Models Comparison

In this sub-section, results of simulation based on the proposed physics-based ECMs of Li-ion battery will be compared with those obtained using two electrochemical models, that of the SPM and a pseudo-two-dimensional (P2D) electrochemical model. P2D model is based on a complex partial differential algebraic equation system which has to be solved using specific solver. P2D model is well-established and is known to be accurate. Unfortunately the time-step used to solve the P2D model has to be sufficiently small to ensure numerical accuracy. Hence solution time tends to be high. Nevertheless, P2D model is used in this study as it can serve as the benchmark for the developed ECMs. Details of the P2D model used can be found in [42].

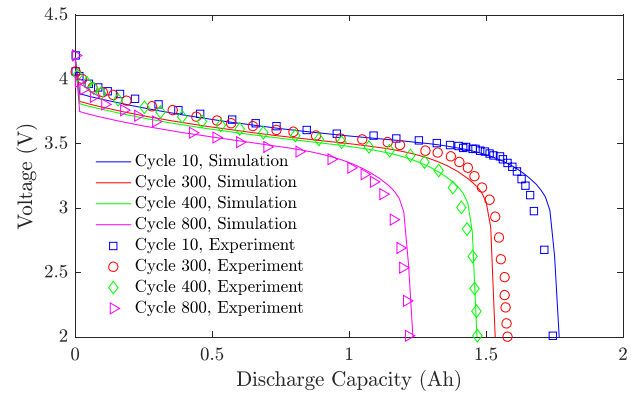


Fig. 8. Comparison of experimental and simulation results. Experimental data are obtained from [43]. The battery is cycled with the constant current-constant voltage (CC-CV) charging and constant current discharging protocol.

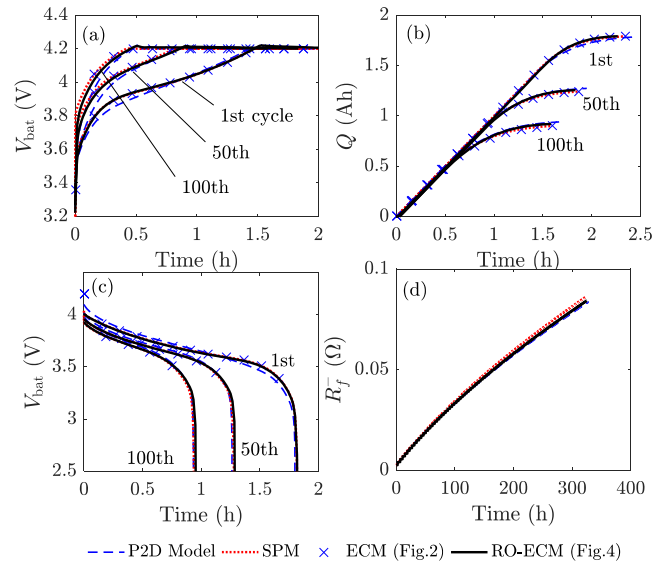


Fig. 9. Comparison of simulation results obtained from P2D model, SPM, developed ECM and RO-ECM: (a) and (b) are for CC-CV charging mode; (c) is for constant current discharge; (d) is the variation of film resistance R_f vs. battery operation time.

All the models are implemented in MATLAB/Simulink on a PC with Intel Core i7-4790 CPU@ 3.60 Hz and 16GB RAM, with the fixed-step discrete solver selected. The similar CC-CV cycling protocol and the 1.8 Ah $LiCoO_2$ battery alluded to in Sub-section 5.1 are again used in this sub-section. During the CV stage, the terminal voltage was regulated using a feedback control scheme. The battery parameters are as given in Table A.1 in Appendix A, while the degradation parameters are adjusted to accelerate the aging effect. The step size for SPM and 4th-order ECM are limited to 5 s to avoid computational instability. While for the RO-ECM, a step size of 60 s is selected due to the limitation of the feedback CV controller, but not due to the model itself.

Fig. 9 shows the comparison of the simulation results obtained from P2D, SPM and the developed ECMs. Fig. 9(a) and Fig 9(b) shows the battery terminal voltage profile and the charging capacity at the end of the 1st, 50th and 100th cycles of the CC-CV charging process. Fig. 9(b) shows the charging capacity is about 1.8 Ah for the 1st cycle charging process. However, the charging capacity is drastically reduced by a

factor of 2 in the 100th cycle. This observation is confirmed by the SPM and P2D model. During the discharging stage, Fig. 9(c) shows that the time to reach the cut-off voltage predicted by the ECMs is in excellent agreement with that obtained using the electrochemical models. Perhaps more importantly, the figure shows that after some 1.5 hours of the discharging process during the 1st cycle, the battery is seen to have reached the knee-point of the discharge curve beyond which the voltage reduces at a most rapid rate. At the end of the 100th cycle, however, the corresponding discharge time is predicted to be only some 0.9 hour before the voltage collapse occurs. This is again in excellent agreement with that given by the electrochemical models.

Unlike the empirical ECMs referred to in Section 1, a distinct advantage of the proposed physics-based ECMs allows the changes in the parametric values of the circuit elements to be updated automatically as the battery degrades. Fig. 9(d) provides such an example in which the growth of the SEI resistance R_f is evaluated and is seen to have reached about 0.084 Ω after 300 hours of operation. The figure shows the irreversible growth is also demonstrated in the P2D model. Although not presented in the figure, it is found that at the end of the simulation, the battery total series resistance is about 0.091 Ω without consideration of the electrolyte resistance R_e . This confirms R_f has indeed become the dominant component of the battery resistance at this stage.

Table 2 compares the time step used in the simulation, the execution time required using the P2D model, the SPM and the developed ECM and RO-ECM, and the root-mean-square errors (RMSEs) of the terminal voltage spanning over the entire 100 cycles of the cyclic testing of the battery. The RMSEs were evaluated by comparing the results obtained using these models with that based on the well-recognized P2D model. The errors are due to the assumption made in SPM and the ECMs in that the electrolyte concentration is constant. Nevertheless, all the voltage RMSEs are well below 1%. The RMSEs calculated when comparing the results of battery charging capacity and SEI film resistance obtained from the SPM and ECMs against the bench-mark P2D model are all less than 0.3%. Based on these observation, it is concluded that the ECM and RO-ECM have performed as well as the SPM, while the RO-ECM has the added advantage that it has reduced the solution time by a factor of about 40, as compared to that required by the SPM.

Table 2
Comparison of Models Complexity and Performance.

Model	P2D	SPM	ECM	RO-ECM
Time Step	0.5 s	5 s	5 s	60 s
Execution Time	559 s	36.3 s	25.9 s	0.91 s
RMSE Fig. 9(a)	-	0.50%	0.51%	0.56%
compared Fig. 9(b)	-	0.15%	0.15%	0.16%
to P2D Fig. 9(c)	-	0.59%	0.60%	0.65%
(%) Fig. 9(d)	-	0.22%	0.23%	0.25%

5.3 Model Application: Impacts of Degradation on Long-Term Battery Energy Storage System Operations

The purpose of this sub-section is to demonstrate insights which can be gained from using the proposed physics-based RO-ECM of the Li-ion battery. In the illustrative example used herewith, a 91-MWh BESS is to smoothen the output power of a hypothetical 100-MW wind farm. The objective of this

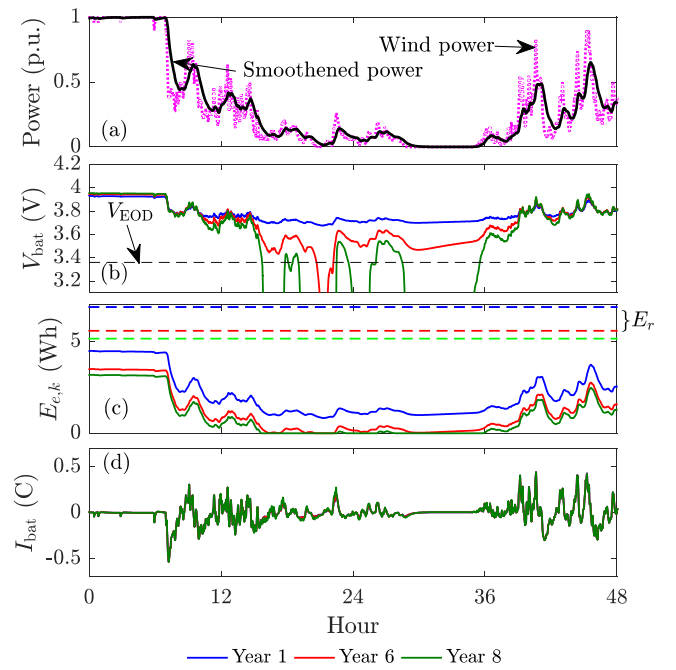


Fig. 10. (a) Generated wind and output powers of wind farm; (b) – (d) Results of simulation study based on the proposed physics-based RO-ECM: 93rd–94th days of the 1st, 6th and 8th years of battery operations. Also shown in (c) are the feasible energy capacity $E_{r,k}$ (dashed lines) of the selected days and years.

study is to investigate the performance of the BESS over the long term, as part of a system planning study based on historical wind resource data observed at the wind farm so that suitable BESS capacity and operational strategy can be determined. Accordingly, a set of wind speed data over a selected year was taken from [44] to generate the wind power at the hypothetical wind farm. The output power of the wind farm is to be smoothened by the buffering actions of the BESS. A sample of the wind and smoothened powers is shown in Fig 10(a). The difference between the generated wind power and the smoothened power forms the input power $P_{bat}(t)$ to the BESS over the year. In this study, the yearly $P_{bat}(t)$ is then applied repeatedly to the BESS over an eight-year period. In this way, a meaningful evaluation of the BESS performance, impacted solely due to cell degradation over the long term, can be made. The electrochemical characteristics and parameters of the individual battery cells which constitute the BESS are again correspond to those given in [28] and are listed in Appendix A. All the battery cells are assumed identical and each cell is represented by the RO-ECM shown in Fig. 4. The circuit parameters and FOZ are obtained as functions of the SOC, in the form of look-up tables which are updated hourly ($T_d = 3600$ s) in the simulation. For a step size $T_s = 60$ s, it requires 23 s to yield the results shown in Figs. 10–12 for the 8-year BESS operations.

Fig. 10 shows the sample profiles of several Li-ion cell variables on the 93rd–94th days of the 1st, 6th and 8th year of BESS operations. From Fig. 10(b), it can be seen that the operating range of the cell terminal voltage V_{bat} increases as the BESS usage progresses. The loss of cell energy storage capacity and the increase in R_f with the battery usage account for the larger voltage variations. Fig. 10(c) shows the exportable energy $E_{e,k}$ of the BESS over the 2-day interval, as well as the feasible energy capacity $E_{r,k}$ (dashed lines). It can

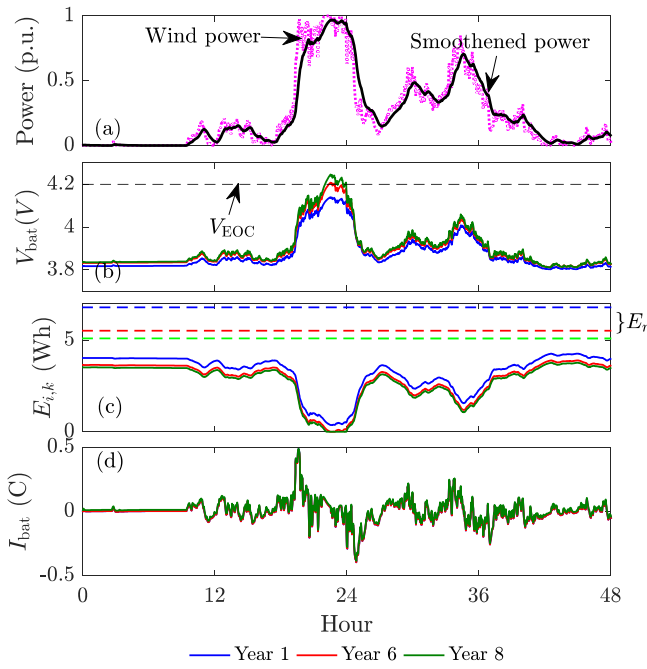


Fig. 11. (a) Generated wind and output powers of wind farm; (b) – (d) Results of simulation study based on the proposed physics-based RO-ECM: 218th–219th days of the 1st, 6th and 8th years of battery operations. Also shown in (c) are the feasible energy capacity $E_{r,k}$ (dashed lines) of the selected days and years.

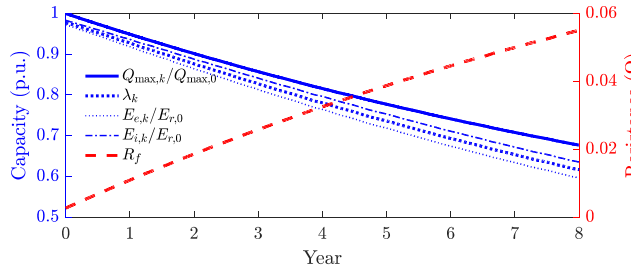


Fig. 12. $Q_{\max,k}/Q_{\max,0}$, $R_{f,k}$ and λ_k over the long term

be seen that $E_{e,k}$ remains positive between the 14th – 36th hours of the selected 2-day interval in the 1st year of the BESS operations. $E_{e,k}$ starts to reach the zero level over the same period when the battery is in the 4th year of operations. In the 8th year and over the same period, the battery over-discharges during most of the time. This undesirable state can be readily identified in Fig. 10(b) whereby the cell terminal voltage has dropped below the set limit V_{EOD} . The ability of the BESS to release energy to the grid is quite limited by this stage. Similarly, Fig. 11 shows selected BESS variables over another two-day period (218th–219th days) of the same three years. Fig. 11(c) illustrates the amount of energy $E_{i,k}$ that can be absorbed by the BESS. It can be seen that approximately between the 22–24th hours of the two-day period, $E_{i,k}$ falls from about 0.84 Wh/cell in the 1st year, to about 0.32 Wh/cell in the 4th year, and reaches zero in the 8th year. From Fig. 11(b), it can be seen that V_{bat} in the 8th year has exceeded the upper limit of the terminal voltage V_{EOC} : the BESS is overcharged over these two hours.

Fig. 10(d) and Fig. 11(d) show the battery current C-rate over the selected periods are all under 0.52 C. Although details are not shown here, a statistical analysis carried out on the battery current over the 8-year period establishes that the

maximum current is only 0.73 C and in fact, the probability the current is less than 0.5 C is 0.999. The assumption that the Li-ion battery is operating at low C rate, a situation under which the physics-based ECMs has been developed from the SPM, is therefore valid in this example.

Fig. 12 shows the persistent growth in R_f , the continuous decline in the energy capacity index λ_k , as well as that in the battery Ah charge capacity $Q_{\max,k}$, and the feasibly exportable and importable energies $E_{e,k}$ and $E_{i,k}$ over the 8-year operations. It is interesting to note that the rates of the decline in the capacity-related terms λ_k , $Q_{\max,k}$, $E_{e,k}$ and $E_{i,k}$ and that of the increase in R_f become less pronounced as the BESS ages. This is because the loss of the negative electrode capacity, as illustrated in Fig. 3, has moved the operating range to higher V_1^- region as the degradation progresses. This causes a reduction in the voltage difference $U_{sr,ref} - V_1^-$, which in turn slows down the rate of the side reactions. This interesting observation has also been reported in [28]. Also as shown by λ_k in Fig. 12, at the end of the 8th year, the maximum amount of the stored energy $E_{r,k}$ in $C_{eq,k}$ that can be used during the subsequent continuous loading process is only 60% of that when the battery is at BOL state. It can also be seen from Fig. 12 that the feasibly exportable energy $E_{e,k}$ is always less and the feasibly importable energy $E_{i,k}$. The difference is due to the internal resistive loss in the battery. Indeed, it can be observed from Fig. 12 that the loss increases over time as a result of the persistent increase in R_f and therefore $R_{eq,k}(z)$. Such information can be very useful in the operational planning of the BESS by taking into account the BESS varying energy conversion efficiency over the long term.

In summary, this example serves to show that unlike the empirical ECM, the proposed physics-based RO-ECM allows overcharge/overdischarge conditions and feasible energy storage range to be determined. The model is computationally efficient and can be used to predict the onset of stressed battery operating conditions. Preventive actions can then be taken to ensure the safe and prudent operations of the BESS.

6 Conclusions

A physics-based equivalent circuit models which can be used to assess the long-term performance and to predict the lifetime of grid-connected lithium-ion battery energy storage system have been developed. By taking into account the side reactions into the modelling process, it is shown that the derived battery models yield results which are in good agreement with those obtained from reported test measurements, as well as with those simulation results obtained using the well-established electrochemical P2D and single particle models, but at much reduced computational burden.

The developed physics-based equivalent circuit models provide valuable insights into the internal states of the battery, thus paving the way toward the design of strategies for the safe and judicious operations of the Li-ion energy storage device for system planning. A fruitful topic for future study would be in the integration of the BESS in renewable generation, where there is the need to determine battery power flow control strategy and storage capacity to balance the desire to minimize the rate of the battery degradation against the need to maximize the economic benefits of the BESS utilization.

Table A.1
Li-ion battery parameters.

Sym- bol	Physical Meaning (Unit)	Parameters		
		Positive Electrode (+)	Separator (sep)	Negative Electrode (-)
R_p	particle radius (m)	2×10^{-6}	-	2×10^{-6}
D_s	solid phase diffusion coefficient (m ² /s)	1×10^{-14}	-	3.9×10^{-14}
a	specific surface area of electrode (m ⁻¹)	8.85×10^5	-	7.236×10^5
L	length of the electrode (m)	80×10^{-6}	20×10^{-6}	88×10^{-6}
ε_s	volume fraction of the solid phase	0.59	-	0.49
$c_{s,max}$	theoretical maximum concentration in the solid phase (mol·m ⁻³)	51555	-	30555
$\theta_{0\%}$	stoichiometry for an empty battery at BOL	0.95	-	0.03
$\theta_{100\%}$	stoichiometry for a full battery at BOL	0.4870	-	0.8851
r_{eff}	electrode rate constant (A·m ^{2.5} ·mol ^{-1.5})	2.252×10^{-6}	-	4.854×10^{-6}
r_{f0}	SEI film resistance at BOL (Ω·m ²)	0	-	0.01
κ_{eff}	Effective electrolyte conductivity (S·m ⁻¹)	0.0045	0.0563	0.0113
F	Faraday constant (s·A/mol)		96487	
T	temperature (K)		298.15	
R_g	universal gas constant [J/(K·mol)]		8.314	
r_{col}	current collector resistance (Ω·m ²)		0	
c_e^0	average Li-ion concentration in the electrolyte (mol/m ³)		1000	
A	electrode plate area (m ²)		0.05961	
M_f	average molecular weight of the SEI film (kg/mol)		7.3×10^{-4}	
ρ_f	SEI film density (kg/m ³)		2.1×10^{-3}	
κ_f	SEI film conductivity [1/(m·Ω)]		0.01	
$i_{0,sr}$	exchange current density for side reaction (A/m ²)		^a 2.025×10^{-7} ^b 6.0×10^{-6}	
$U_{sr,ref}$	equilibrium potential of side reaction (V)		0.4	
$Q_{max,0}$	charge capacity at BOL (Ah)		1.8	

a. For Section 5.1

b. For Section 5.2

Acknowledgments

This work was supported by the Australian Research Council Discovery Grant [grant numbers: DP160101325] and Queensland University of Technology.

Appendix A

The electrochemical parametric values of the Li-ion battery models used in this work are obtained from [27, 28] and listed in Table A.1.

Fig. A.1 shows the equilibrium potential vs. stoichiometry function $f_{s\pm}(\theta_{ss}^{\pm})$ of some common types of electrodes for Li-ion battery. These curves were obtained from the literature. The mathematical expressions of the curves can be obtained by curve fitting technique.

In this work, LiCoO₂ (LCO) positive electrode and LiC₆ (graphite) negative electrode are assumed. The corresponding expressions for $f_{s\pm}(\theta_{ss}^{\pm})$ are:

$$f_{s+}(\theta) = \frac{\begin{pmatrix} -4.656 + 88.669\theta^2 - 401.119\theta^4 \\ +342.909\theta^6 - 462.471\theta^8 + 433.434\theta^{10} \end{pmatrix}}{\begin{pmatrix} -1 + 18.933\theta^2 - 79.532\theta^4 + 37.311\theta^6 \\ -73.083\theta^8 + 95.96\theta^{10} \end{pmatrix}} \quad (\text{A.1})$$

$$f_{s-}(\theta) = 0.7222 + 0.1387\theta + 0.029\theta^{0.5} - 0.0172/\theta + 0.0019\theta^{-1.5} + 0.2808\exp(0.9 - 15\theta) - 0.7984\exp(0.4465\theta - 0.4108) \quad (\text{A.2})$$

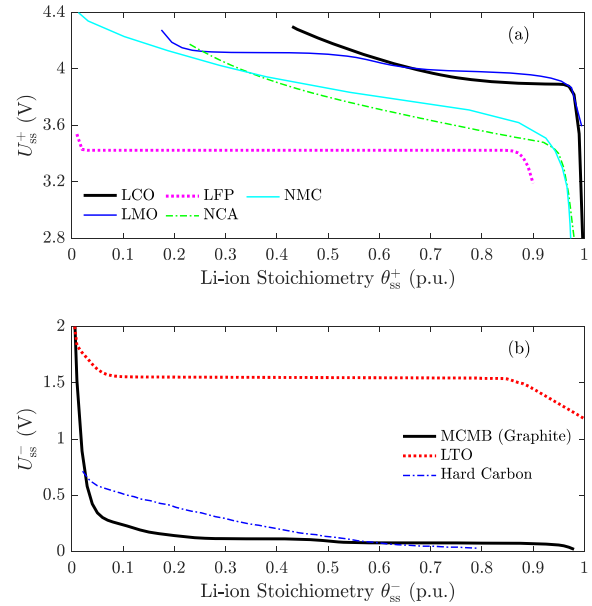


Fig. A.1. Typical relationship between equilibrium potential U_{ss}^{\pm} and stoichiometry θ_{ss}^{\pm} of some common types of positive and negative electrodes. LCO: lithium cobalt oxide; LMO: lithium manganese oxide; NMC: lithium nickel manganese cobalt oxide; LFP: lithium iron phosphate; NCA: lithium nickel cobalt aluminum oxide; MCMB: graphite; LTO: lithium titanate.

Appendix B

First, take the time derivative of (11) and (12) to yield

$$\dot{\theta}_{s,avg}^{\pm} = \frac{1}{f'_{s\pm}(\theta_{s,avg}^{\pm})} \dot{V}_1^{\pm} \quad (\text{B.1})$$

$$\dot{q}_{s,avg}^{\pm}(t) = -\frac{35c_{s,max}^{\pm}}{8R_p^{\pm}f_{s\pm}^{\pm}(\theta_{s,avg}^{\pm})}V_2^{\pm}(t) \quad (B.2)$$

Substituting (13) and (B.1) into (2a) to eliminate $j_1^{\pm}(t)$ and $\theta_{s,avg}^{\pm}(t)$, (14a) is obtained and the expressions of C_1^{\pm} is given in (15).

Next, (2c) can be written as

$$j_1^{\pm}(t) = -\frac{35D_s^{\pm}c_{s,max}^{\pm}}{R_p^{\pm}}\frac{U_{ss}^{\pm}(t)-V_{s,avg}^{\pm}(t)}{f_{s\pm}^{\pm}(\theta_{s,avg}^{\pm})} + 8D_s^{\pm}q_{s,avg}^{\pm}(t) \quad (B.3)$$

where

$$f_{s\pm}^{\pm}(\theta_{s,avg}^{\pm}) = \frac{\partial f_{s\pm}^{\pm}}{\partial \theta_{s,avg}^{\pm}} \approx \frac{U_{ss}^{\pm}(t)-V_{s,avg}^{\pm}(t)}{\theta_{ss}^{\pm}(t)-\theta_{s,avg}^{\pm}(t)} \quad (B.4)$$

Substituting (12) and (13) into (B.4) to produce (14c). The expression of R_1^{\pm} is given in (15).

Finally, substituting (12), (13) and (B.2) into the (2b) to yield the second sub-equation of (14b). The expressions of C_2^{\pm} and R_2^{\pm} are

$$C_2^{\pm} = \frac{7}{12} \frac{AL^{\pm}F\varepsilon_s^{\pm}c_{s,max}^{\pm}}{(-f_{s\pm}^{\pm}(\theta_{s,avg}^{\pm}))} R_2^{\pm} = \frac{-f_{s\pm}^{\pm}(\theta_{s,avg}^{\pm})}{AL^{\pm}F\varepsilon_s^{\pm}c_{s,max}^{\pm}} \frac{2(R_p^{\pm})^2}{35D_s^{\pm}} \quad (B.5)$$

It can be readily shown that $C_2^{\pm} = (7/12)C_1^{\pm}$, $R_2^{\pm} = 6R_1^{\pm}$.

Appendix C

The side-reaction current density J_{sr}^{-} can be expressed as an explicit function of the input current I_{bat} and the stoichiometry θ_{ss}^{-} by solving the nonlinear simultaneous equations (1b), (4), (8) and (9) of SPM, as suggested in [40]

$$J_{sr}^{-} = \frac{\alpha\beta + \alpha\sqrt{\beta^2 + (1-2\gamma\alpha)}}{1-2\gamma\alpha} \quad (C.1)$$

where

$$\alpha = -i_{0,sr}a^{-} \exp\left(\frac{F[U_{sr,ref}^{-} - U_{ss}^{-}(\theta_{ss}^{-}(t))]}{2R_gT}\right)$$

$$\beta = \frac{I_{bat}(t)}{2a^{-}L^{-}Ai_0^{-}(\theta_{ss}^{-}(t))}$$

$$\gamma = \frac{1}{2a^{-}i_0^{-}(\theta_{ss}^{-}(t))}$$

For low-C rate application, $\theta_{ss}^{-} \approx \theta_{s,avg}^{-}$. So it can be expressed as a linear function of process state variable z (i.e. Q_1^{+}) and Q_{loss}^{-} , governed by (24) and (27), viz.,

$$\theta_{ss}^{-}(t) \approx \theta_{s,avg}^{-}(t) = -3600 \frac{Q_{max,0}^{-} - Q_{loss}^{-}(t) - z(t)}{AL^{-}F\varepsilon_s^{-}c_{s,max}^{-}} + \theta_{100\%}^{-} \quad (C.2)$$

Hence, with given Q_{loss}^{-} , side-reaction current $I_{sr}^{-} = AL^{-}J_{sr}^{-}$ can thus be written as an explicit function of z and I_{bat} . This is denoted as $I_{sr}^{-} = f_{sr}(z, I_{bat})$ in (32).

References

[1] IRENA. Battery Storage for Renewables: Market Status and Technology Outlook. IRENA ed. Bonn, Germany: International Renewable Energy Agency; 2015.

- [2] Luo X, Wang J, Dooner M, Clarke J. Overview of current development in electrical energy storage technologies and the application potential in power system operation. *Appl Energy*. 2015;137:511-36.
- [3] Scopelianos S, Fedorowitsch T, Garcia S. Elon Musk's Tesla to build world's biggest lithium ion battery to secure power for South Australia. *ABC News* 2017.
- [4] Hirth L, Ueckerdt F, Edenhofer O. Integration costs revisited – An economic framework for wind and solar variability. *Renew Energy*. 2015;74:925-39.
- [5] Zhao H, Wu Q, Hu S, Xu H, Rasmussen CN. Review of energy storage system for wind power integration support. *Appl Energy*. 2015;137:545-53.
- [6] Li X, Hui D, Lai X. Battery energy storage station (BESS)-based smoothing control of photovoltaic (PV) and wind power generation fluctuations. *IEEE Trans Sustain Energy*. 2013;4:464-73.
- [7] Teleke S, Baran ME, Huang AQ, Bhattacharya S, Anderson L. Control strategies for battery energy storage for wind farm dispatching. *IEEE Trans Energy Convers*. 2009;24:725-32.
- [8] Teleke S, Baran ME, Bhattacharya S, Huang AQ. Optimal control of battery energy storage for wind farm dispatching. *IEEE Trans Energy Convers*. 2010;25:787-94.
- [9] Teleke S, Baran ME, Bhattacharya S, Huang AQ. Rule-based control of battery energy storage for dispatching intermittent renewable sources. *IEEE Trans Sustain Energy*. 2010;1:117-24.
- [10] Yao DL, Choi SS, Tseng KJ, Lie TT. Determination of short-term power dispatch schedule for a wind farm incorporated with dual-battery energy storage scheme. *IEEE Trans Sustain Energy*. 2012;3:74-84.
- [11] Li Q, Choi SS, Yuan Y, Yao DL. On the determination of battery energy storage capacity and short-term power dispatch of a wind farm. *IEEE Trans Sustain Energy*. 2011;2:148-58.
- [12] Yang Y, Li H, Aichhorn A, Zheng J, Greenleaf M. Sizing strategy of distributed battery storage system with high penetration of photovoltaic for voltage regulation and peak load shaving. *IEEE Trans Smart Grid*. 2014;5:982-91.
- [13] Zhang F, Meng K, Xu Z, Dong ZY, Zhang L, Wan C, Liang J. Battery ESS planning for wind smoothing via variable-interval reference modulation and self-adaptive SOC control strategy. *IEEE Trans Sustain Energy*. 2017;8:695-707.
- [14] Bai L, Jiang T, Li F, Chen H, Li X. Distributed energy storage planning in soft open point based active distribution networks incorporating network reconfiguration and DG reactive power capability. *Appl Energy*. 2018;210:1082-91.
- [15] Jannesar MR, Sedighi A, Savaghebi M, Guerrero JM. Optimal placement, sizing, and daily charge/discharge of battery energy storage in low voltage distribution network with high photovoltaic penetration. *Appl Energy*. 2018;226:957-66.
- [16] Khalid M, Aguilera RP, Savkin AV, Agelidis VG. On maximizing profit of wind-battery supported power station based on wind power and energy price forecasting. *Appl Energy*. 2018;211:764-73.
- [17] Wee KW, Choi SS, Vilathgamuwa DM. Design of a least-cost battery-supercapacitor energy storage system for realizing dispatchable wind power. *IEEE Trans Sustain Energy*. 2013;4:786-96.
- [18] Nguyen C-L, Lee H-H, Chun T-W. Cost-optimized battery capacity and short-term power dispatch control for wind farm. *IEEE Trans Ind Appl*. 2015;51:595-606.
- [19] Luo F, Meng K, Dong ZY, Zheng Y, Chen Y, Wong KP. Coordinated Operational Planning for Wind Farm With Battery Energy Storage System. *IEEE Trans Sustain Energy*. 2015;6:253-62.
- [20] Zhang X, Yuan Y, Hua L, Cao Y, Qian K. On Generation Schedule Tracking of Wind Farms With Battery Energy Storage Systems. *IEEE Trans Sustain Energy*. 2017;8:341-53.
- [21] Dufo-López R. Optimisation of size and control of grid-connected storage under real time electricity pricing conditions. *Appl Energy*. 2015;140:395-408.
- [22] Xu B, Oudalov A, Ulbig A, Andersson G, Kirschen D. Modeling of lithium-ion battery degradation for cell life assessment. *IEEE Trans Smart Grid*. 2018;9:1130-40.
- [23] Wang J, Liu P, Hicks-Garner J, Sherman E, Soukiazian S, Verbrugge M, Tataria H, Musser J, Finamore P. Cycle-life model for graphite-LiFePO4 cells. *J Power Sources*. 2011;196:3942-8.
- [24] Zou C, Manzie C, Nesić D. A framework for simplification of PDE-based lithium-ion battery models. *IEEE Trans Control Syst Technol*. 2016;24:1594-609.
- [25] Gu R, Malysz P, Yang H, Emadi A. On the suitability of electrochemical-based modeling for lithium-ion batteries. *IEEE Trans Transport Electrification*. 2016;2:417-31.

- [26] Ramadesigan V, Northrop PWC, De S, Santhanagopalan S, Braatz RD, Subramanian VR. Modeling and simulation of lithium-ion batteries from a systems engineering perspective. *J Electrochem Soc.* 2012;159:R31-R45.
- [27] Santhanagopalan S, Guo Q, Ramadass P, White RE. Review of models for predicting the cycling performance of lithium ion batteries. *J Power Sources.* 2006;156:620-8.
- [28] Ramadass P, Haran B, Gomadam PM, White R, Popov BN. Development of first principles capacity fade model for Li-ion cells. *J Electrochem Soc.* 2004;151:A196-A203.
- [29] Fu R, Choe S-Y, Agubra V, Fergus J. Development of a physics-based degradation model for lithium ion polymer batteries considering side reactions. *J Power Sources.* 2015;278:506-21.
- [30] Smith KA, Rahn CD, Wang C-Y. Model-Based Electrochemical Estimation and Constraint Management for Pulse Operation of Lithium Ion Batteries. *IEEE Trans Control Syst Technol.* 2010;18:654-63.
- [31] Randall AV, Perkins RD, Zhang X, Plett GL. Controls oriented reduced order modeling of solid-electrolyte interphase layer growth. *J Power Sources.* 2012;209:282-8.
- [32] Lawder MT, Suthar B, Northrop PWC, De S, Hoff CM, Leitemann O, Crow ML, Santhanagopalan S, Subramanian VR. Battery energy storage system (BESS) and battery management system (BMS) for grid-scale applications. *Proc IEEE.* 2014;102:1014-30.
- [33] Hesse H, Schimpe M, Kucevic D, Jossen A. Lithium-ion battery storage for the grid-a review of stationary battery storage system design tailored for applications in modern power grids. *Energies.* 2017;10:2107.
- [34] Guo M, Sikha G, White RE. Single-particle model for a lithium-ion cell: thermal behavior. *J Electrochem Soc.* 2011;158:A122-A32.
- [35] Birkel CR, Roberts MR, McTurk E, Bruce PG, Howey DA. Degradation diagnostics for lithium ion cells. *J Power Sources.* 2016;341:1-35.
- [36] Feng X, Sun J, Ouyang M, He X, Lu L, Han X, Fang M, Peng H. Characterization of large format lithium ion battery exposed to extremely high temperature. *J Power Sources.* 2014;272:457-67.
- [37] Smith K, Saxon A, Keyser M, Lundstrom B, Ziwei C, Roc A. Life prediction model for grid-connected Li-ion battery energy storage system. *American Control Conference (ACC).* Seattle, WA, USA: IEEE; 2017. p. 4062-8.
- [38] Delacourt C, Safari M. Life Simulation of a Graphite/LiFePO₄ Cell under Cycling and Storage. *J Electrochem Soc.* 2012;159:A1283-A91.
- [39] Subramanian VR, Diwakar VD, Tapriyal D. Efficient macro-micro scale coupled modeling of batteries. *J Electrochem Soc.* 2005;152:A2002-A8.
- [40] Plett GL. Algebraic solution for modeling SEI Layer growth. *ECS Electrochem Lett.* 2013;2:A63-A5.
- [41] Li Y, Vilathgamuwa DM, Farrell TW, Choi SS, Tran NT. An equivalent circuit model of Li-ion battery based on electrochemical principles used in grid-connected energy storage applications. 3rd IEEE International Future Energy Electronics Conference and ECCE Asia (IFEEC 2017 - ECCE Asia). Kaohsiung, Taiwan: IEEE; 2017. p. 959-64.
- [42] Li Y, Vilathgamuwa M, Farrell T, Choi SS, Tran NT, Teague J. A physics-based distributed-parameter equivalent circuit model for lithium-ion batteries. *Electrochimica Acta.* 2019;299:451-69.
- [43] Ramadass P, Haran B, White R, Popov BN. Mathematical modeling of the capacity fade of Li-ion cells. *J Power Sources.* 2003;123:230-40.
- [44] 1-minute Interval Iowa AWOS data.